

Tunable superconducting diode effect in higher-harmonic InSb nanosheet interferometers

Xingjun Wu,^{1, §} Ji-Yin Wang,¹ Haitian Su,^{2,3} Shili Yan,¹

Dong Pan,^{4,*} Jianhua Zhao,⁴ Po Zhang,^{1,†} and H. Q. Xu^{1,2,‡}

¹Beijing Academy of Quantum Information Sciences, Beijing 100193, China

²Beijing Key Laboratory of Quantum Devices, Key Laboratory for the Physics and Chemistry of Nanodevices, and School of Electronics, Peking University, Beijing 100871, China

³Institute of Condensed Matter and Material Physics, School of Physics, Peking University, Beijing 100871, China

⁴State Key Laboratory of Superlattices and Microstructures, Institute of Semiconductors, Chinese Academy of Sciences, P.O. Box 912, Beijing 100083, China

§ wuxj@baqis.ac.cn, * pandong@semi.ac.cn, † zhangpo@baqis.ac.cn, ‡ hqxu@pku.edu.cn

Superconducting diodes, characterized by the nonreciprocal supercurrent flow, have gained significant attention for their potential in dissipationless electronics. This study presents a superconducting quantum interference device (SQUID) composed of two Al-InSb nanosheet Josephson junctions. Utilizing prepatterned local backgates, we achieve a gate- and flux-tunable superconducting diode with controllable efficiency in both amplitude and sign. Numerical simulations attribute the diode effect to higher harmonics in the current-phase relation. Crucially, fractional Shapiro step experiments provide direct insights into the evolution of these higher harmonics with flux tuning, showcasing significant enhancements in the second-harmonic signatures of the SQUID near half-integer flux quanta. Furthermore, we investigate the microwave-assisted diode response and experimentally show that the polarity of the diode effect can be switched by the microwave power. These results demonstrate the potential of InSb nanosheet-based hybrid devices as highly tunable elements for use in dissipationless electronics.

The superconducting diode effect (SDE) is a nonreciprocal transport phenomenon, analogous to charge transport in semiconductor $p - n$ junctions, where dissipationless superconducting currents flow in one direction while being blocked or partially blocked in the opposite direction. This unique characteristic positions superconducting diodes as promising elements for applications in superconducting electronics, spintronics, and quantum technologies[1–4]. The SDE has recently attracted worldwide attention and has been the subject of study in various superconducting systems, including Josephson junctions (JJs) and junction-free superconductors[5–18]. The microscopic mechanisms underlying the SDE involve intrinsic material properties, including finite-momentum pairing[19–21], the magneto-chiral effect[22], and valley polarization[23], as well as extrinsic factors like trapped vortices and self-inductance[15, 24, 25].

For JJs, the current-phase relation (CPR) is typically expressed as a Fourier series, $I = \sum_n I_n \sin(n\varphi)$, where φ is the phase drop across the junction and I_n represents the current component of the n th harmonic term. A purely sinusoidal CPR results in equal amplitudes of positive and negative critical currents, thus precluding the SDE. However, high-transparency JJs generally possess a non-sinusoidal CPR, and in such higher-harmonic JJs ($n > 1$), a non-zero phase difference δ between harmonics can induce SDE, as illustrated by expressions like $I = I_1 \sin(\varphi) + I_2 \sin(2\varphi + \delta)$ [23, 26]. Achieving such non-zero δ typically requires breaking time-reversal and

inversion symmetries, which can arise from an interplay of external magnetic field with spin-orbit coupling or a nonuniform potential[6, 10, 27, 28].

Nonreciprocal critical currents in SQUIDs have been recognized since the 1970s[25, 29], but they have recently gained renewed attention due to the involvement of high-order harmonics in CPR[30–39]. Theoretical proposals suggest that higher-harmonic CPR in SQUIDs with highly transmissive JJs can significantly affect supercurrent nonreciprocity, with predictions of a butterfly pattern diagram to illustrate diode efficiency[37, 38]. These theoretical frameworks set the stage for experimental investigations into SDE in various hybrid systems with SQUID configurations. Recent experiments have focused on quantum well-based hybrid superconductor-semiconductor interferometers, such as those made from Al-InAs and Al-Ge quantum wells, where gate-tunable $\sin(2\varphi)$ elements are anticipated to enable parity-protected qubits[30–35]. Tuning these diode responses with a microwave field is predicted to yield intriguing results, such as achieving an ideal SDE[32, 38] or even switching the polarity of the diode[40, 41], the latter of which has yet to be reported by experiments. These results offer valuable insights for creating a highly tunable superconducting diode.

InSb nanosheet is a two-dimensional (2D) semiconductor nanostructure developed in recent years[42, 43]. With its strong spin-orbit interaction, small effective mass, large Landé g -factor[42, 44, 45], and 2D geometry, InSb

nanosheets have emerged as a highly promising platform for the development of novel planar hybrid quantum devices[10, 46–48]. While prior studies have predominantly focused on devices incorporating single JJs, including the intrinsic diode effect in InSb nanosheets [10], research on nanosheet-based interferometers remains limited. The development of such interferometers holds the potential to introduce additional tuning knobs, facilitating the exploration of novel hybrid quantum devices on nanosheets.

In our work, we engineered the SDE in an InSb nanosheet interferometer with higher-harmonic junctions. As opposed to the intrinsic diode in single JJs[10], the SDE in a SQUID does not rely on spin-orbit coupling or in-plane Zeeman fields. Instead, tuning the two asymmetric SQUID arms enables a wider range of control over diode rectification efficiency. In the experiment, we demonstrate effective control of the supercurrent in each junction using two pre-patterned local backgates. This enables the realization of a gate- and flux-tunable superconducting diode with a controllable diode efficiency, both in amplitude (up to $\sim 10\%$) and direction. We analyze the mechanism and find that higher-order Josephson harmonics in CPR are indispensable for the SDE. We utilize fractional Shapiro steps to monitor the higher harmonic content in flux-tuning experiments. Notably, we observe significant enhancements in the second-harmonic signatures of the SQUID near half-integer flux quanta. Furthermore, we investigate the microwave response and experimentally demonstrate that the SDE can not only be tuned by microwave power, but also be switched. This may open up new possibilities for application with a microwave-controlled diode effect[40]. Numerical calculations qualitatively support all observations.

Figure 1(a) shows a false-color scanning electron microscope image of an Al-InSb interferometer. Two planar JJs (JJ_1 and JJ_2), each consisting of Al and InSb nanosheets with a gap of about 100 nm, are looped by the Al superconducting wires to form an SQUID (see Supplemental Material for a zoomed-in image of JJ_1 and JJ_2 [49]). The free-standing InSb nanosheets are grown by molecular-beam epitaxy, with a typical thickness of 10 to 100 nm. Details about the material and transport properties have been studied in previous reports[43, 47, 50]. A set of prepatterned metallic (Ti/Au) backgates are fabricated beneath the InSb nanosheets, isolated by a 15 nm HfO_2 dielectric layer. They are used to independently tune the superconductivity of JJ_1 and JJ_2 by applying respective backgate voltages. InSb nanosheets are mechanically transferred by a tip, followed by a standardized aluminum evaporation process. Fabrication details are presented in Supplemental Material[49]. A standard DC measurement is performed in a dilution refrigerator with a base temperature of about 15 mK.

In Fig. 1(c) and 1(d), we present the differential re-

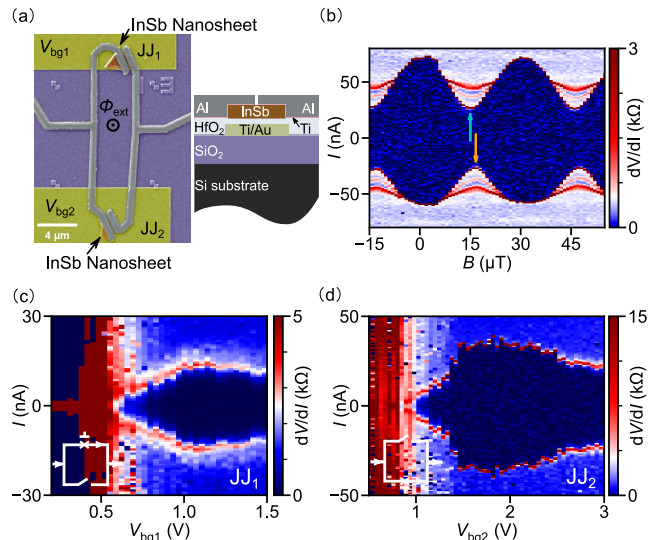


FIG. 1. Device and characterization. (a) False-color scanning electron microscopy image of Al-InSb SQUID and the cross-section of the Al-InSb nanosheet JJ that makes up the SQUID. The brown regular polygon regions are two free-standing InSb nanosheets. (b) Differential resistance dV/dI of the SQUID as a function of bias current I and perpendicular magnetic field B at $V_{bg1} = 1.069$ V and $V_{bg2} = 1.8$ V. The cyan and orange arrows illustrate the extreme positions of the switching and retrapping valleys respectively. (c) and (d) Differential resistance dV/dI as a function of bias current and backgate voltage for JJ_1 and JJ_2 . When one junction is measured, the other is completely pinched off by the corresponding backgate voltage.

sistance of JJ_i ($i = 1, 2$) as a function of the respective backgate voltage V_{bgi} and bias current I . When measuring one JJ, a backgate voltage of 0 V is applied to pinch off the other JJ. The critical current of JJ_1 can be tuned from a pinch-off status at $V_{bg1} \leq 0.5$ V to approximately 15 nA at $V_{bg1} = 1.07$ V, while the critical current of JJ_2 can be tuned from pinch-off at $V_{bg2} \leq 0.9$ V up to 40 nA at $V_{bg2} = 1.8$ V. A slight decrease in the critical current I_c is observed as V_{bg} continues to increase. This could be related to the distribution of carriers at high V_{bg} . At high V_{bg} values, carriers are pushed away from the superconductor-semiconductor interface due to electrostatic potential effects, thereby affecting the superconducting proximity effect and reducing I_c . Additionally, excessive carrier accumulation at high V_{bg} may enhance electron-electron interactions and scattering, which could also contribute to the suppression of I_c . Similar non-monotonic behavior of I_c with V_{bg} has been reported in other JJ systems[51, 52]. Compared to JJ_1 , the stochastic switching current in JJ_2 exhibits a more pronounced response to thermal and charge fluctuations when tuning V_{bg2} , as illustrated in Fig. 1(d).

Figure 1(b) shows the differential resistance of the

SQUID as a function of perpendicular magnetic field B and bias current I at a gate configuration of $V_{bg1} = 1.069$ V and $V_{bg2} = 1.8$ V, where I is swept from negative to positive in the ‘+’ direction. Three main observations are as follows: (1) The SQUID oscillation is periodic with a period of $32 \mu\text{T}$. This periodicity corresponds to an added external flux quantum Φ_0 , which gives the area of the inner loop $S = 64.7 \mu\text{m}^2$. This value is slightly larger than the actual inner area of our SQUID ($S = 55 \mu\text{m}^2$). This discrepancy could be due to the magnetic flux focusing effect or London penetration. (2) A set of fringes emerges in the oscillation valley. The discrete fringes observed may arise from Andreev bound states (ABSs) within the induced superconducting gap or from multiple Andreev reflections. As the critical current at the valley decreases, the finite voltage step at the superconducting transition drops below the bias voltage necessary to access the characteristic energy levels within the sub-gap, thereby facilitating the emergence of these fringes. (3) An asymmetry between the switching and retrapping branches is observed, representing an indirect signature of SDE. Overheating, however, can lead to an artificial SDE: once the junction switches to the resistive state, it fails to return to the superconducting state due to thermal effects until I decreases below the smaller retrapping current, I_{re} , resulting in $I_{re} < I_{sw}$. To exclude this artificial SDE caused by overheating, a standard approach in diode experiments involves comparing the switching current in the ‘+’ direction (I_{sw}^+) with that in the opposite ‘-’ direction (I_{sw}^-), as illustrated in Fig. 2(a).

To quantify SDE, we study I_{sw}^+ and I_{sw}^- obtained in two opposite sweep directions. The red branch in Fig. 2(a) corresponds to the current sweeping from zero to a positive value in the ‘+’ direction, while the blue branch corresponds to sweeping from zero to a negative value in the ‘-’ direction. An asymmetric configuration of the SQUID is established in the measurement using V_{bg1} and V_{bg2} , with $I_{sw1} = 18$ nA and $I_{sw2} = 44$ nA (see Supplemental Material for the determination method of I_{sw1} and I_{sw2} in the SQUID[49]). I_{sw}^+ and $|I_{sw}^-|$ as functions of the external magnetic flux Φ are extracted and shown as green and orange curves, respectively, in Fig. 2(b). A clear asymmetry in the bias current direction is observed, indicating the presence of SDE. The polarity of the SDE changes around $\Phi = 0.5\Phi_0$, as reflected in the diode efficiency η , defined as

$$\eta = \frac{|I_{sw}^+| - |I_{sw}^-|}{|I_{sw}^+| + |I_{sw}^-|} \quad (1)$$

Next, we attempt to understand the origin of the SDE in this experiment. Recognizing that loop inductance can result in an SDE in SQUIDs, we model an inductive SQUID following Ref. 53. The total current I_{tot} passing through the SQUID is the sum of the currents through

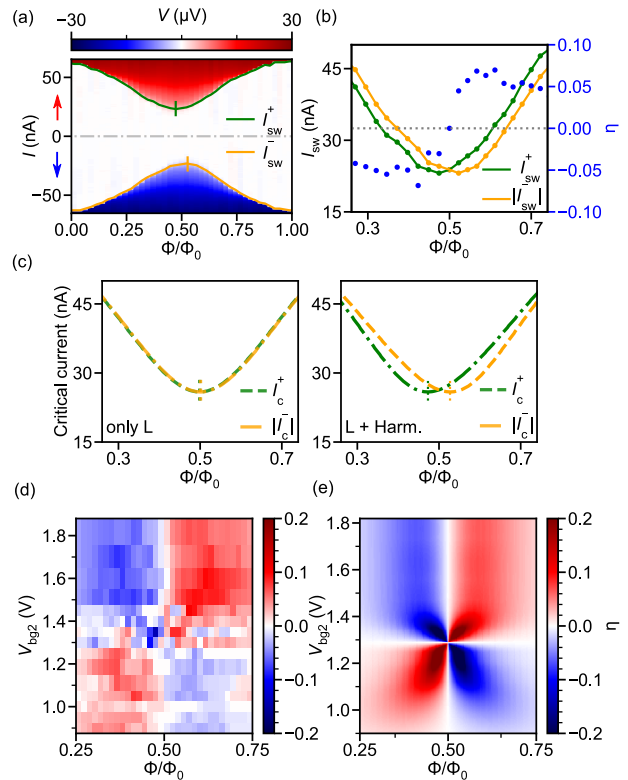


FIG. 2. Gate- and flux-tunable SDE. (a) The measured voltage V as a function of I and Φ/Φ_0 at a gate configuration of $(V_{bg1}, V_{bg2}) = (1.069 \text{ V}, 1.819 \text{ V})$. I is swept from zero to positive values (indicated by the red arrow) in the red branch, and subsequently from zero to negative values (indicated by the blue arrow) in the blue branch, allowing the extraction of switching currents I_{sw}^+ and I_{sw}^- for two opposite sweep directions. (b) I_{sw}^+ and $|I_{sw}^-|$, extracted from panel (a), plotted as a function of Φ/Φ_0 . The blue dotted line corresponds the diode efficiency. (c) I_c^+ and $|I_c^-|$, simulated using two different parameters, as a function of Φ/Φ_0 . Parameters in the left panel consider only a realistic $L = 100$ pH, while parameters in the right include $L = 100$ pH and the first two harmonics (K_1, K_2) = (0.96, 0.04). Parameters $(I_{sw1}, I_{sw2}) = (18 \text{ nA}, 44 \text{ nA})$, obtained at a gate configuration of $(V_{bg1}, V_{bg2}) = (1.069 \text{ V}, 1.819 \text{ V})$, are used for both plots. (d) and (e) Efficiency η as a function of V_{bg2} and Φ/Φ_0 , respectively, obtained from the experiment and theoretical model. Here, V_{bg1} is fixed at 1.069 V. In panel (d), the pixel distribution along the V_{bg2} axis is non-uniform due to unequal spacing in V_{bg2} sampling.

JJ₁ and JJ₂:

$$I_{tot}(\varphi_1, \varphi_2) = I_1(\varphi_1) + I_2(\varphi_2) \quad (2)$$

Here φ_1 and φ_2 represent the phase drops across JJ₁ and JJ₂, respectively. The loop inductance L introduces additional flux into the system, with its magnitude directly

proportional to the circulating current J in the loop:

$$J = (I_1(\varphi_1) - I_2(\varphi_2))/2 \quad (3)$$

$$\varphi_2 - \varphi_1 = 2\pi\Phi_{ext}/\Phi_0 + 2\pi LJ/\Phi_0 \quad (4)$$

where Φ_{ext} indicates a flux induced by the external magnetic field and $\Phi_0 = h/2e$ represents the flux quantum. We disregard inductance asymmetry between branches as they are negligible in our SQUID setup. Given a specific Φ_{ext} , I_{tot}^+ or I_{tot}^- can be determined by identifying the maximum or minimum I_{tot} concerning φ_1 .

To analyze the impact of inductance on the SDE, we first assume a standard sinusoidal CPR for JJ₁ and JJ₂. i.e., $I_1 = I_{sw1}\sin\varphi_1$, $I_2 = I_{sw2}\sin\varphi_2$. A realistic L in SQUID is the sum of the geometric and kinetic inductances, here estimated to be 100 pH (see Supplemental Material for details[49]). The left panel in Fig. 2(c) shows a numerical fit with $L = 100$ pH. We find that, simply including a realistic L does not adequately capture the asymmetry in the switching current observed in the experiment. To address this asymmetry, L should be at least an order of magnitude larger than the realistic value. Thus, the contribution of higher-order harmonics to the SDE is significant in our SQUID, even if the higher harmonic content is relatively small. For simplicity, we assume that JJ₁ and JJ₂ exhibit the same harmonic content, leading to the CPR:

$$I_1(\varphi_1) = \alpha_1 I_{sw1} \sum_n (-1)^{n+1} K_n \sin(n\varphi_1) \quad (5)$$

$$I_2(\varphi_2) = \alpha_2 I_{sw2} \sum_n (-1)^{n+1} K_n \sin(n\varphi_2) \quad (6)$$

Here, K_n represents the n th harmonic content, and $\alpha_{1,2}$ is a normalized coefficient ensuring $\max[I_1(\varphi_1)] = I_{sw1}$ and $\max[I_2(\varphi_2)] = I_{sw2}$. To simplify the analysis, we focus on the first two harmonics in this study. The right panel in Fig. 2(c) illustrates a numerical fit with $K_1 = 0.96$, $K_2 = 0.04$ and $L = 100$ pH. Incorporating contributions from the first two harmonics, with a small K_2 , effectively captures crucial experimental characteristics.

We now return to quantify the SDE and discuss its dependence on gate voltage and external flux. Our measurements demonstrate that the flux-dependent SDE can be tuned with varying gate voltages (see Supplementary Material for details[49]). To systematically quantify the SDE, we extract η as a function of V_{bg2} and external flux Φ/Φ_0 at $V_{bg1} = 1.069$ V, as depicted in Fig. 2(d). The key observation is that both the magnitude and the sign of η can be tuned by V_{bg2} and Φ/Φ_0 . When $V_{bg2} > 1.3$ V, $\eta < 0$ for $\Phi/\Phi_0 < 0.5$ and $\eta > 0$ for $\Phi/\Phi_0 > 0.5$. Conversely, when $V_{bg2} < 1.3$ V, the scenario is reversed. The experiment yields a maximum $|\eta|$ of around 10%. Numerical simulation results in Fig. 2(e) show η as a function of V_{bg2} and Φ/Φ_0 . In the simulation, we assume the CPR in JJ_{*i*} ($i = 1, 2$) remains in the form of $I_i = \alpha I_{swi}[K_1\sin(\varphi_i) - K_2\sin(2\varphi_i)]$, with $K_1 = 0.96$, K_2

$= 0.04$, and I_{swi} as a gate-dependent switching current in JJ_{*i*}. The experiment and numerical simulation highlight a critical value of $V_{bg2} \approx 1.3$ V, where η changes sign, corresponding to a symmetric SQUID case ($I_{sw1} = I_{sw2}$). The absence of asymmetry between I_{sw1} and I_{sw2} leads to a decrease in $|\eta|$. However, in practical experiments, especially when I_{sw1} and I_{sw2} are nearly equal, fluctuations in diode polarity are more likely to be triggered by the stochastic nature of I_{sw} , as seen at $V_{bg2} \approx 1.3$ V in Fig. 2(d).

The agreement between the experiment results and the theoretical model highlights the critical role of the high-order harmonic term in CPR. While the CPR of single junctions is not measured due to the absence of a reference junction with a significantly larger critical current, the nonsinusoidal CPR in single JJs inevitably contributes to the emergence of high-order harmonics in the SQUID. These harmonics can be effectively investigated through the AC Josephson effect. In an SQUID without high-order harmonics, quantized voltage plateaus (Shapiro steps) appear at $V = N\frac{hf}{2e}$, with N being an integer, h the Planck constant and f the microwave frequency. When the SQUID includes a high-order harmonic term, such as $\sin(n\varphi)$ with $n > 1$, fractional quantized voltage plateaus emerge at $V = \frac{N}{n}\frac{hf}{2e}$. Thus, by monitoring the evolution of these fractional Shapiro steps in flux-tuning experiments, one can gain direct insights into the behavior of the relevant high-order harmonic term in the SQUID.

In the following, we study the microwave response of our system. The microwave is coupled to the sample via an antenna positioned approximately 1 mm away. Due to frequency-dependent coupling and the lack of impedance matching between the antenna and the sample, accurately quantifying the microwave power reaching the sample is challenging. Therefore, as is common in similar experiments, we report only the nominal microwave power output from the generator at room temperature.

Figure 3(a) shows differential resistance dV/dI as a function of microwave power P and bias current I at different Φ_{ext} . The microwave driving frequency is 6 GHz. The minima in the dV/dI curves correspond to the Shapiro steps in the $V-I$ characteristic. The low-order integer Shapiro step regions are marked in Fig. 3(a). Three main observations are as follows: (1) In addition to the integer Shapiro steps, half-integer steps are also observed at zero Φ_{ext} , appearing as dips between adjacent integer Shapiro step lobes. This indicates the presence of higher-order harmonics in our SQUID. (2) As Φ_{ext} is tuned from 0 to $0.5\Phi_0$, the first half-integer Shapiro step region appears between the first Shapiro step lobes of index 0 and ± 1 . At the same time, the zero-voltage region shrinks significantly. These behaviors can also be directly identified by comparing the $V-I$ curves at $\Phi_{ext}/\Phi_0 = 0$ and 0.5 under the same microwave power. As shown in Fig. 3(b),

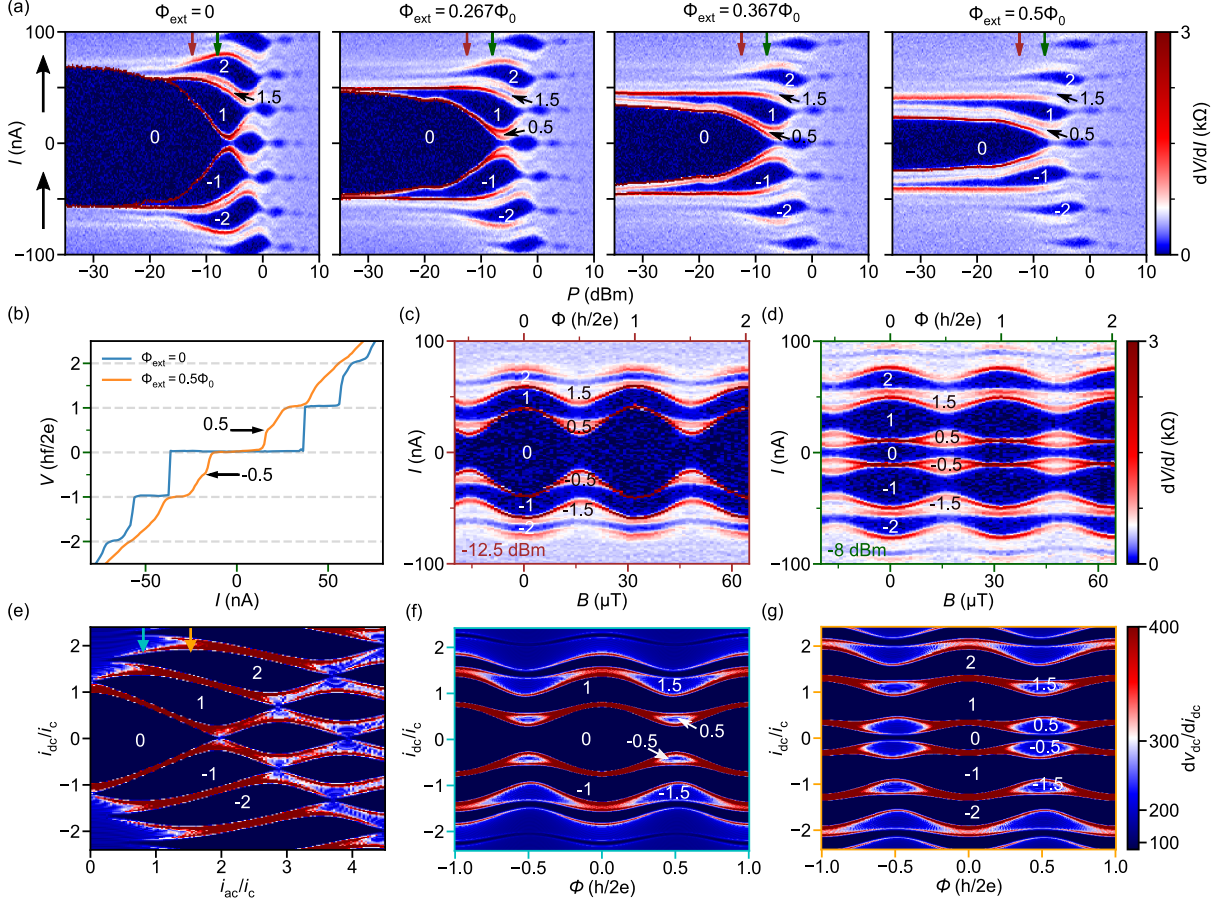


FIG. 3. Enhanced second-harmonic signatures near half-integer flux quanta. (a) Differential resistance dV/dI as a function of I and P when Φ_{ext} is tuned from 0 to $0.5\Phi_0$. The microwave frequency is 6 GHz, and the gate configuration is $V_{bg1} = 1.069$ V and $V_{bg2} = 1.8$ V. The black arrow on the axis indicates the sweeping direction of the dc current bias. The top brown and darkgreen arrows point to the power values of $P = -12.5$ and -8 dBm. (b) Voltage-current curves at $\Phi_{ext} = 0$ and $0.5\Phi_0$, as extracted from panel (a) at $P = -12.5$ dBm. Voltage is normalized to $hf/2e$. Half-integer Shapiro steps appear at $\Phi_{ext} = 0.5\Phi_0$, highlighted by the black arrows. (c-d) Differential resistance dV/dI versus I and Φ at $P = -12.5$ dBm and -8 dBm. The integer and half-integer Shapiro step regions have been labeled, with half-integer steps primarily observed near half-integer flux quanta. (e) Calculated differential resistance map as a function of the dc and ac current bias at $\Phi_{ext} = 0$. Here, a RSJ model is used, disregarding Joule overheating and nonlinear resistance effects. At $i_{ac}/i_c = 0.806$ (cyan arrow) and 1.53 (orange arrow), the differential resistance dV_{dc}/dI_{dc} versus i_{dc} and Φ is plotted in panel (f) and (g), respectively. Parameters used for all simulation plots are $R = 300 \Omega$, $K_1 = 0.96$, $K_2 = 0.04$, $f = 6$ GHz.

when fixing $P = -12.5$ dBm, a weakly developed quantized voltage step at $V = \frac{1}{2} \frac{hf}{2e}$ emerges at $\Phi_{ext} = 0.5\Phi_0$, while a sharp voltage jump occurs instead at $\Phi_{ext} = 0$. (3) Higher-order half-integer Shapiro step regions are expanded by tuning Φ_{ext} to $0.5\Phi_0$. For instance, in the area around $(-10$ dBm, 55 nA) in Fig. 3(a), which corresponds to the Shapiro step of index $3/2$, there is a notable vertical expansion of the Shapiro step region as Φ_{ext} is tuned from 0 to $0.5\Phi_0$.

Studying the Φ_{ext} -dependent Shapiro steps at fixed P provides a comprehensive understanding of the effect of

external flux on higher-order harmonics. Figure 3(c) and 3(d) show the cases of $P = -12.5$ and -8 dBm, respectively. We observe, first, that in Fig. 3(c) and 3(d), the Shapiro step islands, characterized by an index of 0.5 , become apparent at half-integer values of Φ_{ext}/Φ_0 . These islands gradually disappear once Φ_{ext}/Φ_0 deviates from half-integer values. Second, we observe a periodic oscillation of the Shapiro step regions with indices $3/2$ and $5/2$ as a function of Φ_{ext} , with a period of Φ_0 . These half-integer Shapiro step regions reach maxima at half-integer values of Φ_0 and minima at integer values of Φ_0 .

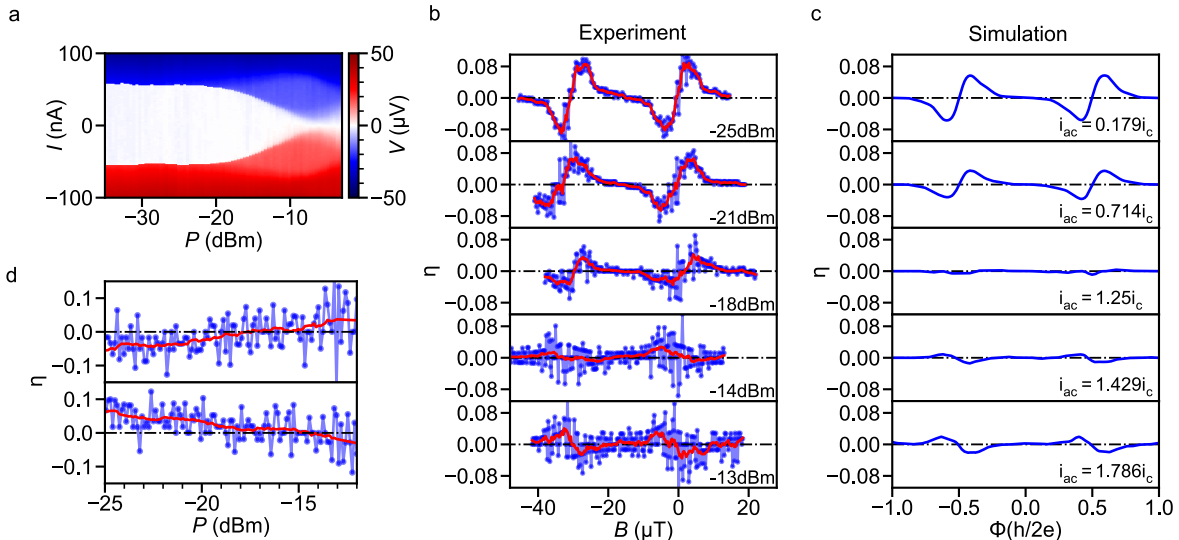


FIG. 4. Tuning diode nonreciprocity with the microwave power at 8 GHz. (a) The voltage drop V across the SQUID as a function of P and I at zero B . (b) The experimental diode efficiency η as a function of B at different P . B is recalibrated for each line by subtracting offsets. (c) The numerically simulated efficiency η as a function of Φ with varying i_{ac} . (d) Efficiency η as a function of P at a fixed Φ , with $\Phi < 0.5\Phi_0$ in the top panel and $\Phi > 0.5\Phi_0$ in the bottom panel. The red curves in panel (b) and (d), fitted to η , are obtained using a Savitzky-Golay filter.

To analyze the dynamics of the SQUID in the microwave field, we consider a resistively shunted junction (RSJ) model with a current bias, disregarding Joule overheating and nonlinear resistance effects. The time-dependent phase difference $\varphi(t)$ and the voltage drop $V(t) = (\hbar/2e)\dot{\varphi}(t)$ are given by

$$\frac{\hbar}{2eR}\dot{\varphi}(t) + I[\varphi(t)] = i_{dc} + i_{ac}\sin(\omega t) \quad (7)$$

Where i_{dc} and i_{ac} are the amplitudes of the dc and ac amplitudes, ω is the microwave frequency, R is a shunt resistance in parallel with the interferometer and $I[\varphi(t)]$ is the total CPR of the interferometer, which, as mentioned above, considers only the first two harmonics. By solving this equation numerically, we find that, despite the simplicity of the model, the results qualitatively capture the main features of this work. Figure 3(e) presents the simulated Shapiro pattern at $\Phi_{ext}/\Phi_0 = 0$ and at a drive frequency of 6 GHz. At $i_{ac}/i_c = 0.806$ and 1.53, indicated by the cyan and orange arrows, the calculated differential resistances dv_{dc}/di_{dc} versus Φ and i_{dc} are depicted in Fig. 3(f) and 3(g). These results agree well with the main features observed in Fig. 3(c) and 3(d).

Next, we discuss the reasons behind the evolution of the half-integer Shapiro steps. Given that the CPR in JJ_i ($i = 1, 2$) follows $I_{JJ_i} = \alpha I_{ci}[K_1\sin(\varphi) - K_2\sin(2\varphi)]$, the CPR of the SQUID at $\Phi_{ext} = 0$ and $0.5\Phi_0$ thus can be

given by

$$I_{\Phi_{ext}=0} = \alpha(I_{c1} + I_{c2})[K_1\sin(\varphi) - K_2\sin(2\varphi)]$$

$$I_{\Phi_{ext}=0.5\Phi_0} = \alpha(I_{c2} - I_{c1})K_1\sin(\varphi) - \alpha(I_{c2} + I_{c1})K_2\sin(2\varphi)$$

By tuning Φ_{ext} , the ratio between the second and first harmonics increases from $\left|\frac{K_2}{K_1}\right|$ at $\Phi_{ext} = 0$ to $\left|\frac{I_{c2} + I_{c1}}{I_{c2} - I_{c1}}\right|\left|\frac{K_2}{K_1}\right|$ at $\Phi_{ext} = 0.5\Phi_0$. The enhanced second-harmonic content influences the behavior of the half-integer Shapiro steps near $\Phi_{ext} = 0.5\Phi_0$. In the symmetric limit where $I_{c1} = I_{c2} = I_c$, the first harmonic can be completely suppressed at $\Phi_{ext} = 0.5\Phi_0$, with the second harmonic ($I_{\Phi_{ext}} = -2\alpha K_2 I_c \sin(2\varphi)$) contributes to the supercurrent. This regime corresponds to the transport of pairs of Cooper pairs. However, the relatively small magnitude of the second harmonics makes the direct observation of the second harmonic-induced supercurrent component particularly challenging. In addition, we have noticed that in Fig. 3, under the influence of DC bias, magnetic flux, and microwave power, we did not observe the pronounced asymmetric Shapiro step formation or the displaced Shapiro steps phenomenon that is typically seen in JJ array structures[54] or asymmetric SQUID ratchets[38, 55]. The absence of such clear asymmetry is related to the relatively low content of higher-order harmonic terms in the CPR of the SQUID (see Supplemental Material for a simulation with a higher $\left|\frac{K_2}{K_1}\right|$).

In the final section of this study, we delve into the diode response by tuning microwave powers. The theoretical investigations have revealed that as power levels increase, the efficiency η can potentially reach 100% [38, 41, 56]. This ideal diode has been experimentally reported [18, 32]. A further theoretical study recently revealed that tuning i_{ac} may also switch the diode polarity [40, 41], but this has not yet been experimentally reported.

In Fig. 4(a), we measure the voltage drop V across the SQUID under microwave irradiation with a drive frequency of $f = 8$ GHz. As the microwave power P increases, the switching current is gradually suppressed. At a constant P , we measure the $V - I$ curves under different B by sweeping the current in two opposite directions, thus obtaining I_{sw}^+ and I_{sw}^- as functions of B . Consequently, we determine η by utilizing I_{sw}^+ and I_{sw}^- , and plot them against B in Fig. 4(b). Despite the presence of noise in the signal, it is clear that the diode polarity, in addition to being periodically influenced by B (or magnetic flux ϕ), is also governed by P . A switch in diode polarity occurs when P is around -14 dBm. The reproducibility of this result can be partially validated by observing similar behavior over two consecutive magnetic flux quantum periods. At the same time, we notice that the fluctuations in η become more pronounced at elevated P . This can be partly attributed to the increased stochasticity of the switching current resulting from thermal fluctuations associated with higher microwave power. Indeed, it is more likely due to the suppression of I_{sw}^+ and I_{sw}^- at elevated power P . When the switching current is smaller, identical fluctuation levels in I_{sw}^+ and I_{sw}^- lead to more pronounced fluctuations in η , given that $\eta = \frac{|I_{sw}^+| - |I_{sw}^-|}{|I_{sw}^+| + |I_{sw}^-|}$. To further rule out the possibility of experimental artifacts, we directly sweep P while setting B to $\Phi < 0.5\Phi_0$ and $\Phi > 0.5\Phi_0$ to measure the diode polarity switching, as illustrated in Fig. 4(d). The diode polarity switching can be observed around -15 dBm. Figure 4(c) presents a numerically simulated result using the RSJ model with previously obtained parameters. i_{ac} are selected at values before reaching the first node of the zeroth Shapiro step lobe. The simulated result qualitatively agrees with the experimental observations. As i_{ac} is tuned from $0.179i_c$ to $1.786i_c$, the sign of η changes accordingly. The sign-reversal of the diode efficiency can be intuitively understood as follows: In the fast-driving limit and considering the zero-voltage step, the amplitudes of the Josephson harmonics K_n in the CPR are modulated by the zeroth Bessel function of the first kind [41]. Specifically, $K_1 \propto J_0(i_{ac}/\omega)$, $K_2 \propto J_0(2i_{ac}/\omega)$. As i_{ac} increases, both K_1 and K_2 can change signs, leading to a sign change of the diode efficiency. The microwave-controlled switching of diode polarity offers new possibilities for distinguishing 4π -periodic topological Josephson junctions in asymmetric SQUIDs [40].

In conclusion, we have developed a gate- and flux-

tunable superconducting diode utilizing a SQUID composed of aluminum and InSb nanosheets. Theoretical analyses indicate that higher harmonics dominate the SDE rather than L . Fractional Shapiro step experiments demonstrate the evolution of these higher harmonics with flux tuning, showing significant enhancements in the second-harmonic signatures of the SQUID near half-integer flux quanta, as confirmed by numerical simulations. Furthermore, by integrating numerical calculations with microwave experiments, we show that the diode polarity can be switched by tuning the microwave power in SQUIDs. These findings present an exciting perspective for exploring highly tunable superconducting diodes on nanosheet-based interferometers and realizing a parity-protected qubit. They may also have potential applications in discerning 4π -periodic Josephson junctions.

AUTHOR CONTRIBUTIONS

H.Q.X. supervised the project. X.W., H.S., and S.Y. fabricated devices. X.W. and J.-Y.W. performed measurements. X.W. did the simulation. D.P. and J.Z. developed the nanosheet material. X.W., P.Z., and H.Q.X. analyzed the data and wrote the manuscript with inputs from all the authors.

ACKNOWLEDGEMENTS

This work is supported by the NSFC (Grant Nos. 92165208, 12004039, 11874071, 92365103, 12374480, 12374459, 61974138 and 92065106). D.P. acknowledges the support from Youth Innovation Promotion Association, Chinese Academy of Sciences (Nos. 2017156 and Y2021043).

DATA ANALYSIS AND DATA AVAILABILITY

The raw data and the analysis files are available at <https://doi.org/10.5281/zenodo.13268561>

-
- [1] A. I. Braginski, Superconductor electronics: Status and outlook, *J Supercond Nov Magn* **32**, 23 (2019).
 - [2] G. Wendin, Quantum information processing with superconducting circuits: a review, *Rep. Prog. Phys.* **80**, 106001 (2017).
 - [3] J. Linder and J. W. Robinson, Superconducting spintronics, *Nat. Phys.* **11**, 307 (2015).
 - [4] R. Cai, I. Žutić, and W. Han, Superconductor/ferromagnet heterostructures: a platform for superconducting spintronics and quantum computation, *Adv. Quantum Technol.* **6**, 2200080 (2023).

- [5] F. Ando, Y. Miyasaka, T. Li, J. Ishizuka, T. Arakawa, Y. Shiota, T. Moriyama, Y. Yanase, and T. Ono, Observation of superconducting diode effect, *Nature* **584**, 373 (2020).
- [6] G. Mazur, N. van Loo, D. van Driel, J.-Y. Wang, G. Badawy, S. Gazibegovic, E. Bakkers, and L. Kouwenhoven, The gate-tunable josephson diode, arXiv preprint arXiv:2211.14283 (2022).
- [7] Y. M. Itahashi, T. Ideue, Y. Saito, S. Shimizu, T. Ouchi, T. Nojima, and Y. Iwasa, Nonreciprocal transport in gate-induced polar superconductor *sr tio3*, *Sci. Adv.* **6**, eaay9120 (2020).
- [8] J.-X. Lin, P. Siriviboon, H. D. Scammell, S. Liu, D. Rhodes, K. Watanabe, T. Taniguchi, J. Hone, M. S. Scheurer, and J. Li, Zero-field superconducting diode effect in small-twist-angle trilayer graphene, *Nat. Phys.* **18**, 1221 (2022).
- [9] C. Baumgartner, L. Fuchs, A. Costa, S. Reinhardt, S. Gronin, G. C. Gardner, T. Lindemann, M. J. Manfra, P. E. Faria Junior, D. Kochan, J. Fabian, N. Paradiso, and C. Strunk, Supercurrent rectification and magnetochiral effects in symmetric josephson junctions, *Nat. Nanotechnol.* **17**, 39 (2022).
- [10] B. Turini, S. Salimian, M. Carrega, A. Iorio, E. Strambini, F. Giazotto, V. Zannier, L. Sorba, and S. Heun, Josephson diode effect in high-mobility insb nanoflags, *Nano Lett.* **22**, 8502 (2022).
- [11] H. Wu, Y. Wang, Y. Xu, P. K. Sivakumar, C. Pasco, U. Filippozzi, S. S. Parkin, Y.-J. Zeng, T. McQueen, and M. N. Ali, The field-free josephson diode in a van der waals heterostructure, *Nature* **604**, 653 (2022).
- [12] F. K. de Vries, E. Portolés, G. Zheng, T. Taniguchi, K. Watanabe, T. Ihn, K. Ensslin, and P. Rickhaus, Gate-defined josephson junctions in magic-angle twisted bilayer graphene, *Nat. Nanotechnol.* **16**, 760 (2021).
- [13] J. Díez-Mérida, A. Díez-Carlón, S. Yang, Y.-M. Xie, X.-J. Gao, J. Senior, K. Watanabe, T. Taniguchi, X. Lu, A. P. Higginbotham, K. T. Law, and D. K. Efetov, Symmetry-broken josephson junctions and superconducting diodes in magic-angle twisted bilayer graphene, *Nat. Commun.* **14**, 2396 (2023).
- [14] M. Trahms, L. Melischek, J. F. Steiner, B. Mahendru, I. Tamir, N. Bogdanoff, O. Peters, G. Reecht, C. B. Winkelmann, F. von Oppen, and K. J. Franke, Diode effect in josephson junctions with a single magnetic atom, *Nature* **615**, 628 (2023).
- [15] A. Sundaresh, J. I. Väyrynen, Y. Lyanda-Geller, and L. P. Rokhinson, Diamagnetic mechanism of critical current non-reciprocity in multilayered superconductors, *Nat. Commun.* **14**, 1628 (2023).
- [16] S. Matsuo, T. Imoto, T. Yokoyama, Y. Sato, T. Lindemann, S. Gronin, G. C. Gardner, M. J. Manfra, and S. Tarucha, Josephson diode effect derived from short-range coherent coupling, *Nat. Phys.* **19**, 1636 (2023).
- [17] N. Lotfizadeh, W. F. Schiela, B. Pekerten, P. Yu, B. H. Elfeky, W. M. Strickland, A. Matos-Abiague, and J. Shabani, Superconducting diode effect sign change in epitaxial al-inas josephson junctions, *Commun. Phys.* **7**, 120 (2024).
- [18] H. Su, J.-Y. Wang, H. Gao, Y. Luo, S. Yan, X. Wu, G. Li, J. Shen, L. Lu, D. Pan, J. Zhao, P. Zhang, and H. Q. Xu, Microwave-assisted unidirectional superconductivity in al-inas nanowire-al junctions under magnetic fields, *Phys. Rev. Lett.* **133**, 087001 (2024).
- [19] B. Pal, A. Chakraborty, P. K. Sivakumar, M. Davydova, A. K. Gopi, A. K. Pandeya, J. A. Krieger, Y. Zhang, M. Date, S. Ju, N. Yuan, N. B. M. Schröter, L. Fu, and S. S. P. Parkin, Josephson diode effect from cooper pair momentum in a topological semimetal, *Nat. Phys.* **18**, 1228 (2022).
- [20] N. F. Yuan and L. Fu, Supercurrent diode effect and finite-momentum superconductors, *Proc. Natl. Acad. Sci.* **119**, e2119548119 (2022).
- [21] M. Davydova, S. Prembabu, and L. Fu, Universal josephson diode effect, *Sci. Adv.* **8**, eabo0309 (2022).
- [22] H. F. Legg, D. Loss, and J. Klinovaja, Superconducting diode effect due to magnetochiral anisotropy in topological insulators and rashba nanowires, *Phys. Rev. B* **106**, 104501 (2022).
- [23] J.-X. Hu, Z.-T. Sun, Y.-M. Xie, and K. T. Law, Josephson diode effect induced by valley polarization in twisted bilayer graphene, *Phys. Rev. Lett.* **130**, 266003 (2023).
- [24] D. Suri, A. Kamra, T. N. Meier, M. Kronseder, W. Belzig, C. H. Back, and C. Strunk, Non-reciprocity of vortex-limited critical current in conventional superconducting micro-bridges, *Appl. Phys. Lett.* **121**, 102601 (2022).
- [25] T. A. Fulton, L. N. Dunkleberger, and R. C. Dynes, Quantum interference properties of double josephson junctions, *Phys. Rev. B* **6**, 855 (1972).
- [26] B. Zhang, Z. Li, V. Aguilar, P. Zhang, M. Pendharkar, C. Dempsey, J. S. Lee, S. D. Harrington, S. Tan, J. S. Meyer, M. Houzet, C. J. Palmstrom, and S. M. Frolov, Evidence of ϕ_0 -josephson junction from skewed diffraction patterns in sn-insb nanowires (2024), arXiv:2212.00199 [cond-mat.mes-hall].
- [27] A. Rasmussen, J. Danon, H. Suominen, F. Nichele, M. Kjaergaard, and K. Flensberg, Effects of spin-orbit coupling and spatial symmetries on the josephson current in sns junctions, *Phys. Rev. B* **93**, 155406 (2016).
- [28] T. Yokoyama, M. Eto, and Y. V. Nazarov, Anomalous josephson effect induced by spin-orbit interaction and zeeman effect in semiconductor nanowires, *Phys. Rev. B* **89**, 195407 (2014).
- [29] T. Fulton and R. Dynes, Current-phase relations in superconducting bridges, *Phys. Rev. Lett.* **25**, 794 (1970).
- [30] C. Ciaccia, R. Haller, A. C. Drachmann, T. Lindemann, M. J. Manfra, C. Schrade, and C. Schönenberger, Gate-tunable josephson diode in proximitized inas supercurrent interferometers, *Phys. Rev. Res.* **5**, 033131 (2023).
- [31] C. Ciaccia, R. Haller, A. C. Drachmann, T. Lindemann, M. J. Manfra, C. Schrade, and C. Schönenberger, Charge-4e supercurrent in a two-dimensional inasal superconductor-semiconductor heterostructure, *Commun. Phys.* **7**, 1 (2024).
- [32] M. Valentini, O. Sagi, L. Baghumyan, T. de Gijssel, J. Jung, S. Calcaterra, A. Ballabio, J. Aguilera Servin, K. Aggarwal, M. Janik, and et al., Parity-conserving cooper-pair transport and ideal superconducting diode in planar germanium, *Nat. Commun.* **15**, 169 (2024).
- [33] M. Gupta, G. V. Graziano, M. Pendharkar, J. T. Dong, C. P. Dempsey, C. Palmstrøm, and V. S. Pribiag, Gate-tunable superconducting diode effect in a three-terminal josephson device, *Nat. commun.* **14**, 3078 (2023).
- [34] T. W. Larsen, M. E. Gershenson, L. Casparis, A. Kringhøj, N. J. Pearson, R. P. McNeil, F. Kuemmeth, P. Krogstrup, K. D. Petersson, and C. M. Marcus, Parity-protected superconductor-semiconductor qubit, *Phys.*

- Rev. Lett. **125**, 056801 (2020).
- [35] A. Leblanc, C. Tangchingchai, Z. S. Momtaz, E. Kiyooka, J.-M. Hartmann, G. T. Fernandez-Bada, Z. Scherübl, B. Brun, V. Schmitt, S. Zihlmann, R. Maurand, E. Dumur, S. De Franceschi, and F. m. c. Lefloch, From nonreciprocal to charge-4e supercurrent in ge-based josephson devices with tunable harmonic content, Phys. Rev. Res. **6**, 033281 (2024).
- [36] P. Zhang, A. Zarassi, L. Jarjat, V. V. de Sande, M. Pendharkar, J. S. Lee, C. P. Dempsey, A. P. McFadden, S. D. Harrington, J. T. Dong, H. Wu, A. H. Chen, M. Hocevar, C. J. Palmström, and S. M. Frolov, Large second-order Josephson effect in planar superconductor-semiconductor junctions, SciPost Phys. **16**, 030 (2024).
- [37] Y. V. Fominov and D. S. Mikhailov, Asymmetric higher-harmonic squid as a josephson diode, Phys. Rev. B **106**, 134514 (2022).
- [38] R. S. Souto, M. Leijnse, and C. Schrade, Josephson diode effect in supercurrent interferometers, Phys. Rev. Lett. **129**, 267702 (2022).
- [39] S. Reinhardt, T. Ascherl, A. Costa, J. Berger, S. Gronin, G. C. Gardner, T. Lindemann, M. J. Manfra, J. Fabian, D. Kochan, *et al.*, Link between supercurrent diode and anomalous josephson effect revealed by gate-controlled interferometry, Nat. Commun. **15**, 4413 (2024).
- [40] J. J. Cuzzo, W. Pan, J. Shabani, and E. Rossi, Microwave-tunable diode effect in asymmetric squids with topological josephson junctions, Phys. Rev. Res. **6**, 023011 (2024).
- [41] R. Seoane Souto, M. Leijnse, C. Schrade, M. Valentini, G. Katsaros, and J. Danon, Tuning the josephson diode response with an ac current, Phys. Rev. Res. **6**, L022002 (2024).
- [42] M. De La Mata, R. Leturcq, S. R. Plissard, C. Rolland, C. Magén, J. Arbiol, and P. Caroff, Twin-induced insb nanosails: A convenient high mobility quantum system, Nano Lett. **16**, 825 (2016).
- [43] D. Pan, D. X. Fan, N. Kang, J. H. Zhi, X. Z. Yu, H. Q. Xu, and J. H. Zhao, Free-standing two-dimensional single-crystalline insb nanosheets, Nano Lett. **16**, 834 (2016).
- [44] H. A. Nilsson, P. Caroff, C. Thelander, M. Larsson, J. B. Wagner, L.-E. Wernersson, L. Samuelson, and H. Xu, Giant, level-dependent g factors in insb nanowire quantum dots, Nano Lett. **9**, 3151 (2009).
- [45] Z. Lei, C. A. Lehner, E. Cheah, C. Mittag, M. Karalic, W. Wegscheider, K. Ensslin, and T. Ihn, Gate-defined quantum point contact in an insb two-dimensional electron gas, Phys. Rev. Res. **3**, 023042 (2021).
- [46] F. K. de Vries, M. L. Sol, S. Gazibegovic, R. L. M. o. h. Veld, S. C. Balk, D. Car, E. P. A. M. Bakkers, L. P. Kouwenhoven, and J. Shen, Crossed andreev reflection in insb flake josephson junctions, Phys. Rev. Res. **1**, 032031 (2019).
- [47] N. Kang, D. Fan, J. Zhi, D. Pan, S. Li, C. Wang, J. Guo, J. Zhao, and H. Xu, Two-dimensional quantum transport in free-standing insb nanosheets, Nano Lett. **19**, 561 (2019).
- [48] A. Iorio, A. Crippa, B. Turini, S. Salimian, M. Carrega, L. Chirolli, V. Zannier, L. Sorba, E. Strambini, F. Giazotto, *et al.*, Half-integer shapiro steps in highly transmissive insb nanoflag josephson junctions, Phys. Rev. Res. **5**, 033015 (2023).
- [49] See Supplemental Material at URL-will-be-inserted-by-publisher for the loop inductance estimation, device fabrication, numerical simulation, and additional data for the device.
- [50] X. Wu, H. Su, C. Zeng, J.-Y. Wang, S. Yan, D. Pan, J. Zhao, P. Zhang, and H. Q. Xu, Superconducting switching jump induced missing first shapiro step in al-insb nanosheet josephson junctions (2024), arXiv:2403.07370 [cond-mat.supr-con].
- [51] S. Yan, H. Su, D. Pan, W. Li, Z. Lyu, M. Chen, X. Wu, L. Lu, J. Zhao, J.-Y. Wang, *et al.*, Supercurrent, multiple andreev reflections and shapiro steps in inas nanosheet josephson junctions, Nano Lett. **23**, 6497 (2023).
- [52] C.-Z. Li, A.-Q. Wang, C. Li, W.-Z. Zheng, A. Brinkman, D.-P. Yu, and Z.-M. Liao, Fermi-arc supercurrent oscillations in dirac semimetal josephson junctions, Nat. Commun. **11**, 1150 (2020).
- [53] C. D. Tesche and J. Clarke, Dc squid: Noise and optimization, J. Low Temp. Phys. **29**, 301 (1977).
- [54] B. Chesca, M. Gaifullin, D. John, J. Cox, S. Savel'ev, and C. Mellor, The influence of magnetic vortices motion on the inverse ac josephson effect in asymmetric arrays, Appl. Phys. Lett. **121**, 162601 (2022).
- [55] I. Zapata, R. Bartussek, F. Sols, and P. Hänggi, Voltage rectification by a squid ratchet, Phys. Rev. Lett. **77**, 2292 (1996).
- [56] J. Clarke and A. I. Braginski, *The SQUID handbook: Applications of SQUIDS and SQUID systems* (John Wiley & Sons, 2006).